Journal of Power Sources 196 (2011) 4290–4297

Contents lists available at ScienceDirect

Journal of Power Sources

journal homepage: www.elsevier.com/locate/jpowsour

Oxygen reduction reaction increased tolerance and fuel cell performance of Pt and Ru_xSe_y onto oxide–carbon composites

Laure Timperman, Aldo S. Gago, Nicolas Alonso-Vante*

Laboratory of Electrocatalysis, UMR-CNRS 6503, University of Poitiers, 40 Av. Recteur Pineau, F-86022 Poitiers, France

ARTICLE INFO

Article history:
Received 31 July 2010
Received in revised form 24 October 2010
Accepted 17 November 2010
Available online 24 November 2010

Keywords:
Oxide–carbon composites
Oxygen reduction
Formic acid
Methanol
Fuel Cell
LFFC

ABSTRACT

Pt and Ru_xSe_y nanoparticles were selectively deposited onto oxide sites of oxide–carbon composite substrates using the photo-deposition process and compared to conventional carbon support materials. The oxide was essentially anatase phase. Cyclic voltammetry and rotating disk electrode measurements for the oxygen reduction reaction (ORR) in formic acid containing-electrolyte showed a tolerance improvement for ORR of Pt supported on composite substrates. This positive substrate effect on platinum, turned out not to be favorable for Ru_xSe_y catalyst centers. On the other hand, the methanol tolerance for ORR was increased for both nanostructured materials supported on the oxide–carbon composite. Single H_2/O_2 fuel cell results were in agreement with half-cell electrochemical measurements on Pt, showing an improvement of the power density when using the oxide–carbon as substrate for the cathode. The composites were evaluated as cathode catalysts of an HCOOH laminar-flow fuel cell (LFFC) in which commercial Pd/C was used as an anode catalyst. The cathodes with Ru_xSe_y and Pt supported on TiO_2/C improved the specific power density by 15% and 24%, respectively, with respect to carbon as support.

1. Introduction

Nanoparticulate catalysts are supported on substrates of various natures for their use in catalysis, as well as electrocatalysis. Of particular interest is the development or modification of the most popular one: carbon (e.g., Vulcan XC-72) for technical anode or cathode electrodes for low temperature fuel cells. Chemical modification of carbon nanotubes [1–3] or nanostructured carbon [4–12] has been undertaken. Another strategy to stabilize the support is to develop metal–oxide substrates as reported for SiO_2 [13], NbO_2 [14], MnO_x [15], WO_x [16,17], SnO_2 [18] and TiO_x [15,19–28]. Pt deposited on such substrates shows an increase of the activity for the oxygen reduction reaction (ORR) as compared to Pt/C. These substrates also exhibit an enhancement of stability [22,24], and an improvement of tolerance towards carbon monoxide [17,18,29,30] and methanol [20,28,29,31–33]. Recently, it has been reported that Pd nanoparticles supported on carbon-modified TiO_2 (rutile) showed a higher activity for formic acid electrooxidation than Pd/C [34]. In this sense, fuel cell performances were also improved according to the increase of tolerance and activity for ORR.

On the other hand, micro-direct methanol fuel cells (μDMFCs) are the most attractive alternative to replace polymer lithium-ion batteries for powering portable electronics (e.g., laptops, cell phones, smart-phones, and tablet computers) [35,36]. However, their commercialization is still hindered by a number of basic problems such as methanol-crossover [37]. To overcome this issue, novel membranes with less methanol permeability or the modification of existing ones are being developed [38,39]. Nevertheless, no significant improvement on the development of alternative electrolyte membranes has been obtained so far. Laminar-flow fuel cells (LFFC), also called microfluidic fuel cells, are one alternative to μDMFCs for powering portable devices [40]. These fuel cells relay on the use of micro-channels to carry the fuel and the electrolyte-oxidant separately and thus without mixing. However, as the hydraulic diameter of the channels is reduced and its length is enlarged, fuel cross-over negative effects are evident [41]. Consequently the performance of this kind of cells is also diminished. Ru_xSe_y has been tested as cathode catalyst in DMFC, LFFC [42] and mixed reactant fuel cells [43]. Such chalcogenide catalyst has a comparable activity to Pt catalyst and a good performance for the ORR even at high concentrations of fuel. Ru_xSe_y particles were also deposited onto metal–oxide substrates and showed an enhancement of the ORR activity [16,25]. Other catalyst materials such as transition metal chalcogenides: Pt_xS_y and Co_xSe_y demonstrated to be methanol tolerant [44–46] and selective to the oxygen reduction reaction (ORR).

This work focuses on the activity for ORR and the tolerance, towards organic molecules such as formic acid and methanol, of Pt and Ru_xSe_y deposited onto oxide–carbon substrate by photo-deposition. The performance of each catalyst is further proved

* Corresponding author. Tel.: +33 54945 3625; fax: +33 54945 3580.
E-mail address: Nicolas.Alonso.Vante@univ-poitiers.fr (N. Alonso-Vante).

0378-7753/$ – see front matter © 2010 Elsevier B.V. All rights reserved.
doi:10.1016/j.jpowsour.2010.11.083

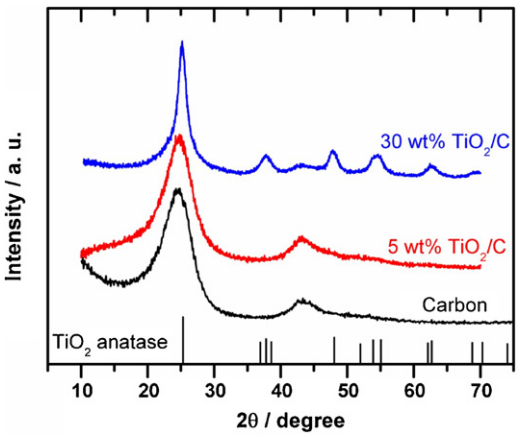

Fig. 1. XRD patterns of 5 wt% TiO_2/C annealed 400 °C-2 h and carbon. Vertical bars on the bottom represent the diffraction peaks positions of TiO_2 anatase.

on single H_2/O_2 fuel cells, and LFFC measurements were undertaken.

2. Experimental

2.1. Synthesis of M/TiO_2/C (M = Ru or Pt)

Oxide–carbon composite substrate was first prepared via a chemical route [25]. The carbon Vulcan XC-72 (200 mg) was ultrasonically stirred with propan-2-ol ("isopropanol") during 2 h. The desired amount of titanium isopropoxide, chemical precursor of TiO_2, was then added in the carbon containing suspension, and stirred during 1 h. Water was finally added, in excess, to hydrolyze the titanium isopropoxide to TiO_2 (anatase form), see Fig. 1, and the obtained suspension was stirred during 24 h. This process was performed at a temperature of 0 °C. The resulting powder was collected after filtration, and then washed with pure water and dried in vacuum. Using this procedure, various oxide-loading composites were prepared. Fig. 1 shows characteristic XRD patterns of carbon, 5 and 30 wt% TiO_2/C after annealing at 400 °C under air. With 5 wt% TiO_2, the diffraction peaks corresponding to anatase are embedded into the carbon matrix. These peaks clearly emerge with higher oxide composition, cf. structural factors of anatase. This was previously confirmed by wide angle XRD measurements [26]. In this work we will focus on the use of 5 wt% oxide–carbon composite.

Platinum and ruthenium nanoparticles were, thereafter, photodeposited via UV-light [25–27]. The Ru/5 wt% TiO_2/C sample was further selenized using the process described by Zaikovskii et al. [47]. In short, Ru/TiO_2/C powder was dispersed into propan-2-ol/water solution by stirring for 30 min. SeO_2 powder was added and the suspension was stirred for 4 h at room temperature. The mass of SeO_2 was calculated in order to obtain Ru_xSe_y ($x \sim 2$ and $y \sim 1$). The powder was obtained after evaporation of the solvent and dried under vacuum. Then it was heat-treated under hydrogen at 200 °C during 1 h, in order to obtain stable Ru_xSe_y/5 wt% TiO_2/C catalysts. For the sake of comparison, Pt/C and Ru_xSe_y/C were also synthesized. The former via the carbonyl method [26,27,48], and the latter using an environmental friendly method [49,50].

2.2. Electrochemical measurements

The electrochemical measurements were performed at 25 °C, using a potentiostat in a thermostated three-electrode cell. A plate of glassy carbon (GC) served as counter electrode, and a reversible hydrogen electrode (RHE) connected to the working electrode compartment through a Luggin capillary, in 0.5 M H_2SO_4 aqueous solution electrolyte, as the reference electrode. A GC rotating disk electrode (0.07 cm^2 geometric surface area) was used as a working electrode where the catalytic powders were deposited from inks, which were prepared by mixing 10 mg of catalyst (8 wt% Pt/C and 8 wt% Pt/TiO_2/C) in 0.25 mL Nafion® (5 wt% in water/aliphatic alcohol solution (Aldrich)) and 1.25 mL ultra pure water, in an ultrasonic bath for 1 h. 3 μL of the catalyst ink were deposited onto the glassy carbon electrode (0.07 cm^2) and dried under nitrogen atmosphere.

Cyclic voltammograms were performed in nitrogen-aturated electrolyte, from 0.05 to 1.2 V/RHE for Pt and from 0.9 to 0.05 V/RHE for Ru_xSe_y catalysts at 50 mV s^{-1}. 20 cycles were necessary to stabilize the system. Linear current–potential curves, for ORR, were recorded after from 1.0 to 0.2 V/RHE for Pt (and from 0.9 to 0.2 V/RHE for Ru_xSe_y), in oxygen-saturated electrolyte at different angular scan rates. Cyclic voltammograms were also recorded in nitrogen-saturated formic acid 5 M or methanol 5 M in H_2SO_4 0.5 M with the same starting and stopping potential for these catalysts. ORR curves were also performed for these samples in oxygen-saturated formic acid 5 M or methanol 5 M in H_2SO_4 0.5 M at different angular rates, in order to evaluate the tolerance to pollutants during the oxygen reduction reaction.

Impedance spectroscopy measurements were recorded for the same materials, using a bi-potentiostat BioLogic SP300. Impedance data were recorded in the range of frequency of 100 kHz–0.1 Hz, as function of applied electrode potential from 0.1 to 0.8 V/RHE every 0.2 V and with a sinus amplitude of 7.1 mV (5 mV rms).

2.3. H_2/O_2 fuel cell measurements

H_2/O_2 fuel cell measurements were performed on single cells provided with 8 wt% Pt/C, and 8 wt% Pt/5 wt% TiO_2/C cathode catalysts. One should note that platinum mass loading is the same since Pt:C equals to Pt:(C + oxide) ratio. Commercial 30 wt% Pt/C E-TEK was used as an anode catalyst with a mass loading of 0.4 mg cm^{-2}. The mass loading at the cathode was 0.16 mg cm^{-2} for 8 wt% Pt/C, and 8 wt% Pt/5 wt% TiO_2/C and also 0.4 mg cm^{-2} for 8 wt% Pt/5 wt% TiO_2/C. The 5 cm^2 electrode surface was deposited on Nafion® 212 membranes. All tests were performed at 80 °C with a flow rate of O_2 of 100 mL min^{-1} and 200 mL min^{-1} for H_2. The home-made catalysts were air-brushed deposited directly onto the Nafion® membranes.

2.4. Laminar-flow fuel cell measurements

A cell design similar to the one described in [51–53] was used for our laminar-flow fuel cell tests. As separator, a Millipore GSWP 200 μm filter was used to minimize the fuel crossover. Each channel was 0.6 mm high, 2.2 mm wide and 28 mm long. The pressure of O_2 on top of the cathode was 1 bar. 5 M HCOOH (Alf Aesar 97%) was used as fuel in 0.5 M H_2SO_4. Both streams were introduced into the LFFC using a syringe pump. The flow rate of the inlet streams was 0.5 mL min^{-1}. The cell operated at room temperature.

Catalysts' suspensions were prepared sonicating the appropriated amount of powder catalyst with 1500 μL of ultra-pure water, 300 μL of Nafion® and 200 μL of propan-2-ol for 1 h. 30 wt% Pd/C E-TEK was used as the anode catalyst. The suspensions with Pt-based catalysts were painted on TGP-H-120 Toray paper. The whole painting process was done at 85 °C to allow the suspension to dry quickly. The Toray paper was weighed before and after to determine the amount of deposited catalyst (Δm). The measured polarization curves were normalized to 1 mg catalyst per unit area (cm^2). For Pd and Ru_xSe_y catalysts, thinner Toray (TGP-H-60) paper was used to improve diffusion species into the electrode. However, less catalyst was deposited on this electrode since most of the suspension passed through it.

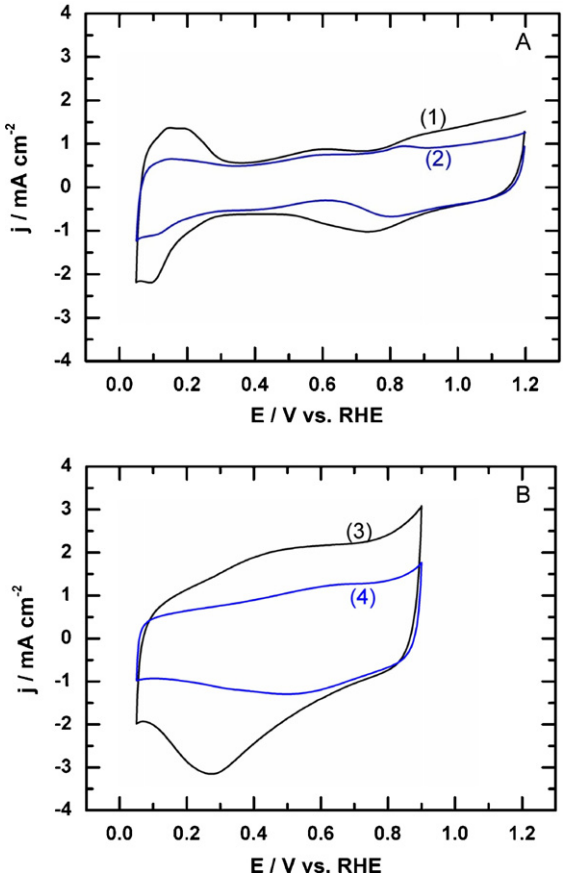

Fig. 2. Cyclic voltammogramms of (A) 8 wt% Pt/C (1) and 8 wt% Pt/5 wt% TiO_2/C (2) and of (B) 15 wt% Ru_xSe_y/C (3) and 15 wt% Ru_xSe_y/5 wt% TiO_2/C (4) in nitrogen-saturated H_2SO_4 0.5 M at 25 °C. Scan rate of 50 mV s^{-1}.

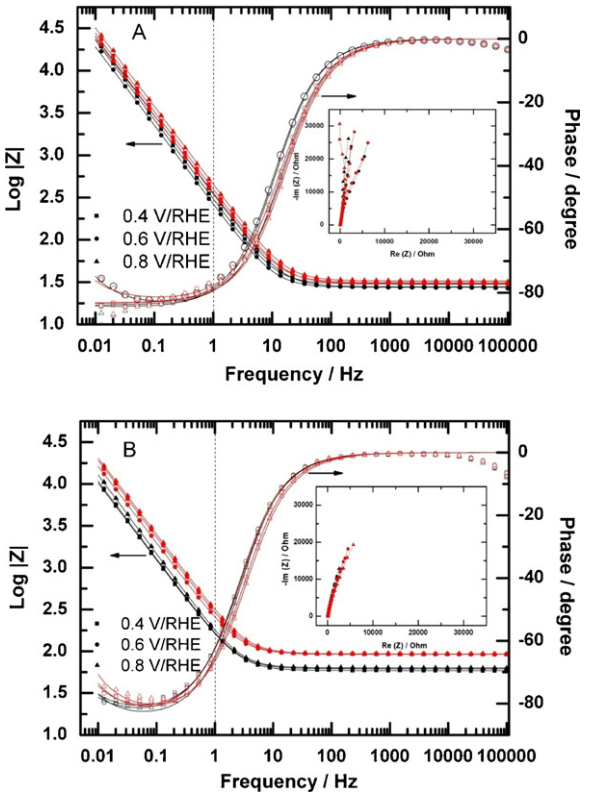

Fig. 3. Bode plot from impedance spectroscopy measurements on (A) 8 wt% Pt/C (black) and 8 wt% Pt/5 wt% TiO_2/C (red) and on (B) 15 wt% Ru_xSe_y/C (black) and 15 wt% Ru_xSe_y/5 wt% TiO_2/C (red) in nitrogen-saturated H_2SO_4 0.5 M at 25 °C. The symbols correspond to experimental points and the full lines correspond to the fittings at 0.4, 0.6, and 0.8 V/RHE. The inset of figures A and B show the Nyquist plots for the same conditions. (For interpretation of the references to color in this figure legend, the reader is referred to the web version of the article.)

The LFFC polarization curves, obtained by measuring current and cell potential as a function of a loading resistance, varied from 1 MΩ to 0.1 Ω. The anode, E_{ano}, and cathode, E_{cat}, potentials were measured separately using an RHE with the Luggin capillary at the outlet of each electrode. A digital multimeter (Fluke 113 A) connected in parallel with a 1 MΩ was used to measure the potential of each electrode. The cell voltage ($E_{cell} = E_{cat} - E_{an}$) was measured with another digital multimeter (Agilent).

3. Results and discussion

3.1. Interfacial behavior of catalysts

Fig. 2A and B depicts the cyclic voltammograms of 8 wt% Pt/C and 8 wt% Pt/5 wt% TiO_2/C and 15 wt% Ru_xSe_y/C and 15 wt% Ru_xSe_y/5 wt% TiO_2/C, respectively. The curves 1 and 2 (Fig. 2A) clearly reveal the characteristic of platinum nanoparticles, e.g., hydrogen adsorption and desorption (between 0.05 and 0.30 V/RHE), platinum oxidation and reduction of platinum oxide (0.75 V/RHE). As previously shown [26], the region of hydrogen adsorption and desorption exhibits lower current density for Pt deposited on the oxide–carbon composite than on carbon alone. One can also note that the double layer induced by the support is lower for Pt supported on the oxide–carbon composite, than on carbon alone. The same effect is also observed for the Ru_xSe_y. The curves of Fig. 2B show the characteristic reduction wave centered at 0.30 V/RHE for 15 wt% Ru_xSe_y/C catalysts. This latter is shifted to 0.55 V/RHE on 15 wt% Ru_xSe_y/5 wt% TiO_2/C. The presence of the oxide and the synthesis by photo-deposition reveal a surface modification of the metal centers. To better visualize such phenomenon, impedance spectroscopy measurements were performed on the same conditions operating for the cyclic voltammogram experiments at different electrode potentials. Fig. 3A and B represents typical Bode plots obtained at 0.4, 0.6 and 0.8 V/RHE, and the corresponding Nyquist plot, in the inset, with the same measurements conditions. Bode plot reveals a phase shift at frequency higher than 10 kHz. This small phase shift, 5–8° at 100 kHz, could not be eliminated by further decreasing the cell time constant. The frequency response of 8 wt% Pt/C and 8 wt% Pt/5 wt% TiO_2/C is fairly similar (Fig. 3A). For some samples, the Nyquist plot reveals a change of time constant at frequency lower than 0.1 Hz. However, using a simple fitting R_1–R_2Q_p circuit to fit the curves allowed for the resistance and the capacitance evaluation. The parameters R_1, R_2 and Q_p, stand for series, parallel resistance and a constant phase element, respectively. From this latter:

$$C = \frac{(RQ)^{1/a}}{R}$$

where α is a constant which is less than 1, $\alpha = 1$ for a pure capacitor. The average resistance R_1 for 8 wt% Pt/C and 8 wt% Pt/5 wt% TiO_2/C is ca. 28.5 Ω and 31.6 Ω, respectively. This small difference apparently does not add an ohmic drop that may affect the current–potential characteristics shape. However, for Ru_xSe_y (Fig. 3B), indeed, 59.6 Ω and 91.6 Ω were obtained, respectively, for 15 wt% Ru_xSe_y/C and for the 15 wt% Ru_xSe_y/5 wt% TiO_2/C. Within the explored potential interval of 0.1–0.8 V/RHE, the frequency response for both catalysts follows the same pattern. On both systems, Fig. 3 shows that the impedance, Log|Z|, increases when nanoparticles are supported on the composites, implying a decrease of Q or C. Table 1 summarizes

Table 1
Capacitance of 8 wt% Pt/C, 8 wt% Pt/5 wt% TiO_2/C, 15 wt% Ru_xSe_y/C and 15 wt% Ru_xSe_y/5 wt% TiO_2/C deduced from cyclic voltammograms (CVs) and from impedance spectroscopy at 0.4 V/RHE.

Catalysts	Capacitance (CVs) (F/g)[a]	Capacitance (CVs) ($\mu F/cm^2_{Pt}$)[b]	Capacitance (impedance) (F/g)[a]	Capacitance (impedance) ($\mu F/cm^2_{Pt}$)[b]
8 wt% Pt/C	42.1 ± 2	7.7 ± 0.3	48.7 ± 1	8.9 ± 0.2
8 wt% Pt/5 wt% TiO_2/C	36.1 ± 2	7.1 ± 0.3	46.2 ± 1	8.4 ± 0.2
15 wt% Ru_xSe_y/C	142 ± 5	–	93.6 ± 3	–
15 wt% Ru_xSe_y/5 wt% TiO_2/C	70 ± 3	–	57.4 ± 1	–

[a] Mass specific capacitance, related to the catalysts mass on the electrode (20 μg).
[b] EAS of platinum determined by CO-stripping.

the capacitance values determined by impedance spectroscopy, as well as by cyclic voltammetry at 0.4 V/RHE (cf. Fig. 2). The reported mass specific capacitance is the contribution of the substrate plus the nanoparticles mass. Taking advantage of the electrochemical active surface (EAS) of platinum nanoparticles determined by CO-stripping [26] the surface specific Pt capacitance was calculated. Both ways of calculation convey to similar results for platinum catalysts. On the other hand, the generated capacitance results on Ru_xSe_y supported catalysts by both methods are more scattered but indicating a same trend, that is, a decrease of the capacitance for catalysts supported on the oxide–carbon composites.

3.2. Evaluation of tolerance to pollutants during ORR

3.2.1. Current–potential curves in formic acid containing electrolyte

The catalysts were evaluated for the oxidation of 5 M formic acid in 0.5 M sulfuric acid electrolyte. Fig. 4A and B depicts the CVs for Pt and Ru_xSe_y catalysts, respectively, supported on TiO_2/C and C. For Pt/C it has been widely accepted in the literature that HCOOH oxidation occurs via a dual-pathway mechanism [54–64], namely, the main one or dehydrogenation reaction that forms directly CO_2:

$$Pt\text{–}(HCOOH)_{ads} \rightarrow CO_2 + 2H^+ + 2e^- \quad (1)$$

and the parallel one or dehydration reaction to form the intermediate species such as $(COOH)_{ads}$, $(COH)_{ads}$, $CH(OH)_2$, etc., leading to the formation of adsorbed CO poisonous species [65]:

$$Pt\text{–}(HCOOH)_{ads} \rightarrow Pt\text{–}(CO)_{ads} + H_2O \quad (2)$$

These adsorbed CO species can be further oxidized to CO_2 by $Pt\text{–}OH_{ads}$ surface species generated from the water dissociation on platinum:

$$Pt + H_2O \rightarrow Pt\text{–}(OH)_{ads} + H^+ + e^- \quad (3)$$

Taking into account these reactions, the curve (1) in Fig. 4A can be analyzed as follows: First, in the positive forward scan, a broad wave (P_1) centered at 0.5 V/RHE is observed, which can be attributed to the formic acid oxidation via the dehydrogenation pathway. The second anodic peak (P_2) centered at 0.92 V/RHE corresponds to the oxidation of $(CO)_{ads}$ generated by the dehydration of formic acid [58,59,64]. Finally, during the backward scan, some CO remain adsorbed until they are oxidized, producing the highest current peak (P_3) at 0.61 V/RHE. These results are in good agreement with the literature [58,59,64].

For Pt/TiO_2/C catalyst, the peak P_1 is almost negligible indicating that the oxidation of HCOOH occurs mainly through the dehydration pathway [64,66,67]. However, this fact should be experimentally confirmed using other techniques such as differential electrochemical mass spectrometry (DEMS) or Fourier transform infrared spectroscopy (FTIR). The value of P_2 is almost the same for Pt/C and for Pt/TiO_2/C, but it is negatively shifted by 30 mV, indicating that the potential barrier for CO oxidation decreased. This is a consequence from the enhanced tolerance of the supported catalyst to CO poisoning. Additionally, the difference

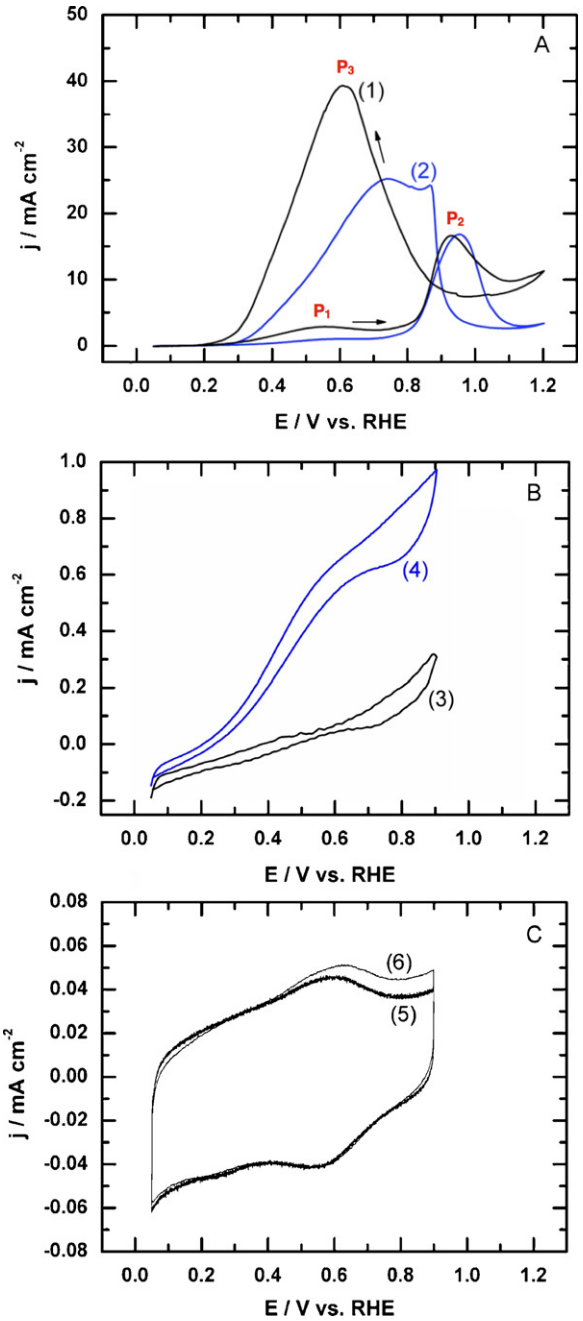

Fig. 4. Cyclic voltammogramms of (A) 8 wt% Pt/C (1) and 8 wt% Pt/5 wt% TiO_2/C (2), of (B) 15 wt% Ru_xSe_y/C (3) and 15 wt% Ru_xSe_y/5 wt% TiO_2/C (4) in nitrogen-saturated 0.5 M H_2SO_4 plus 5 M HCOOH and of (C) the support, 5 wt% TiO_2/C, in 0.5 M H_2SO_4 (5) and in nitrogen-saturated 0.5 M H_2SO_4 plus 5 M HCOOH (6) at 25 °C and at 5 mV s^{-1}, at 25 °C. Scan rate of 5 mV s^{-1}.

between the P_2/P_3 ratio for Pt/TiO_2/C and Pt/C is 0.24. This parameter has been used to evaluate the tolerance of the catalyst towards the electro-oxidation of methanol [29,68]. The peak current ratio is useful to evaluate the tolerance of a catalyst since it measures its ability and efficiency to bind and to oxidize poisoning organic molecules. Therefore, our Pt/TiO_2/C is 57% more tolerant to HCOOH than Pt/C.

The enhancement of the tolerance of Pt/TiO_2/C can be attributed to the synergistic effect between the nanostructured Pt catalyst and the TiO_2 support. Two models can be used to explain this phenomenon, namely, the bifunctional mechanism and the electronic effect [29,69,70]. The bifunctional mechanism is widely used to describe how hydroxyl surface groups participate to oxidize adsorbed CO on Pt–TiO_2 interface. Dissociative adsorption of water molecules on the TiO_2 produces O_2Ti–$(OH)_{ads}$ surface species:

$$O_2Ti + H_2O \rightarrow O_2Ti\text{–}(OH)_{ads} + H^+ + e^- \quad (4)$$

O_2Ti–$(OH)_{ads}$ groups adjacent to Pt nanoparticles can easily oxidize CO bonded on the periphery of Pt atoms by neighboring both entities, i.e., O_2Ti–$(OH)_{ads}$ and Pt–$(CO)_{ads}$:

$$O_2Ti\text{–}(OH)_{ads} + Pt\text{–}(CO)_{ads} \rightarrow CO_2 + Pt + TiO_2 + H^+ + e^- \quad (5)$$

After this reaction, one new Pt free site is created and another OH surface group can be then adsorbed on this Pt site according to reaction (3). The $(OH)_{ads}$ can oxidize another CO group on a neighboring Pt site, producing two new free Pt sites:

$$Pt\text{–}(CO)_{ads} + Pt\text{–}(OH)_{ads} \rightarrow 2Pt + CO_2 + H^+ + e \quad (6)$$

CO oxidation reaction will efficiently continue and the reaction rate will increase as the density of available Pt sites is higher and the coverage of CO diminishes [29].

This simple mechanism can partially explain the tolerance enhancement to $(CO)_{ads}$ poisoning as a consequence of the dehydration of HCOOH. Moreover, TiO_2 cannot only promote CO tolerance via the bifunctional mechanism but the electronic structure modification of Pt, as a result of alloy formation between Ti and Pt [29,69–73].

The strong metal–support interaction (SMSI) between the TiO_2 support and Pt nanoparticles alters the electron density of the valence orbitals [70,71,73]. This hypo–hyper *d*-interaction between the active center and the metal–oxide greatly modifies the electronic structure of the Pt atoms enhancing the electrocatalytic activity towards the oxidation of small organics and the ORR [20,27,74]. The lattice relaxation and the SMSI reduces the $(CO)_{ad}$ binding and activation energy [69]. Therefore, the reactivity and mobility of reactants and organic intermediates on the surface are improved. Stacking faults and micro-strains in the catalyst microstructure also play an important role in the improvement in the catalytic activity [26]. In particular Pt surface atoms at the periphery of Pt nanoparticles are more prone to this electronic effect than those surface atoms that are far away from the Pt–TiO_2 interface. Therefore, as the size of Pt nanoparticles becomes smaller, the number of peripheral Pt active sites increases. This produces an enhancement of the electrocatalytic activity for CO oxidation on the periphery [30]. Additionally, the surface diffusivity of adsorbed organic species on Pt particles can be modified. Using quantum mechanical calculations applied to the support–catalyst cluster interactions and surface diffusivity of the species, Hepel et al. [69] reported that the surface diffusivity of adsorbed $(CO)_{ads}$ on the Pt nanoparticles (<5 nm) is greatly improved. This is consequence of the reduction of the energetic barrier for 2D-diffusion of adsorbed CO (Langmuir–Hinshelwood isotherm) through a new dynamic effect called the cooperative diffusion mechanism [29,69]. The lower adsorbability of CO could also facilitate the desorption and reaction with $(OH)_{ads}$ species via the oxidation with trapped holes at the oxygen vacancies (V_O^{**}) of TiO_{2-x}. The aforementioned

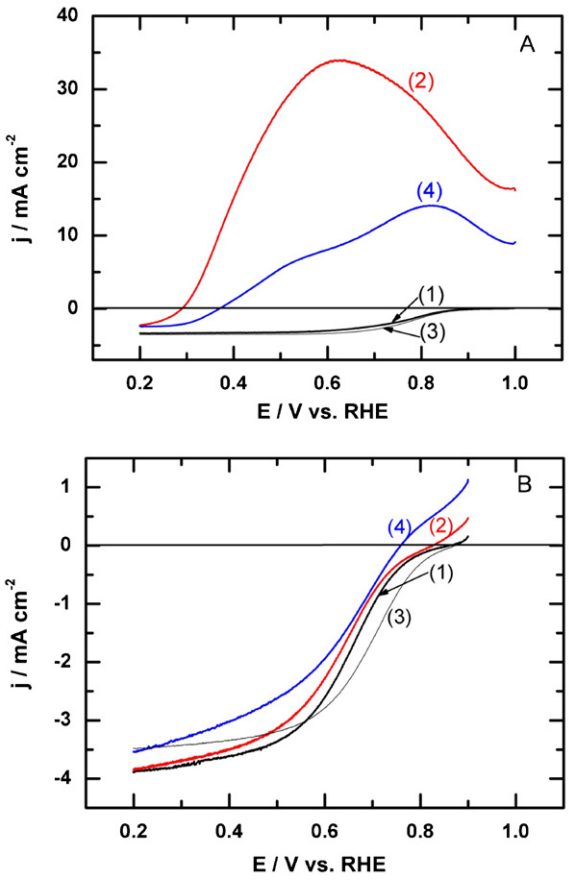

Fig. 5. Oxygen reduction reaction (ORR) curves at 900 rpm on (A) 8 wt% Pt/C (1 and 2) and 8 wt% Pt/5 wt% TiO_2/C (3 and 4) and on (B) 15 wt% Ru_xSe_y/C (1 and 2) and 15 wt% Ru_xSe_y/5 wt% TiO_2/C (3 and 4) in oxygen-saturated 0.5 M H_2SO_4 (curves 1 and 3) and in oxygen-saturated 5 M HCOOH in 0.5 M H_2SO_4 (curves 2 and 4), at 25 °C. Scan rate of 5 mV s^{-1}.

conclusions from the theoretical calculations are in complete agreement with our previous reported results in which we have shown CO tolerance and enhanced ORR activity trough a SMSI between the Pt and TiO_2/C support [26,72].

For Ru_xSe_y catalysts (Fig. 4B), large oxidation waves (under nitrogen) are observed, however the magnitude is determined by the presence of the oxide composite. As shown in Fig. 4C, the oxide–carbon does not induce this effect. It is clear that there is no significant change between curves 5 and 6 which represent respectively the CVs of 5 wt% TiO_2/C in sulfuric acid electrolyte and in 5 M formic acid containing electrolyte. The 15 wt% Ru_xSe_y/5 wt% TiO_2/C is more influenced by the presence of formic acid in the electrolyte than the 15 wt% Ru_xSe_y/C. This enhancement for HCOOH oxidation is mostly due to the bifunctional reaction mechanism from the TiO_2 support, since the SMSI is much weaker for the Ru_xSe_y/TiO_2/C than for Pt/TiO_2/C [75]. Therefore, since the metal substrate interaction (MSI) of Ru_xSe_y/TiO_2/C is weak, it would be expected that the mixed potential, during the ORR in presence of HCOOH, is more negative on Ru_xSe_y/TiO_2/C than on 15 wt% Ru_xSe_y/C, cf. Fig. 5B (curves 2 and 4). However, in electrolytes without HCOOH, the synergistic effect between Ru_xSe_y and TiO_2 is more evident and it should produce a more positive $E_{1/2}$ as observed in Fig. 5 (curves 1 and 3).

Conversely, with respect to the oxidation current density obtained for Ru_xSe_y as compared to Pt, the former catalyst is more tolerant. In fact, this latter is more active for the oxidation of formic acid; the current densities are between 20 and 40 times higher than the values for Ru_xSe_y. This effect was previously reported for methanol tolerance [48–50,76,77].

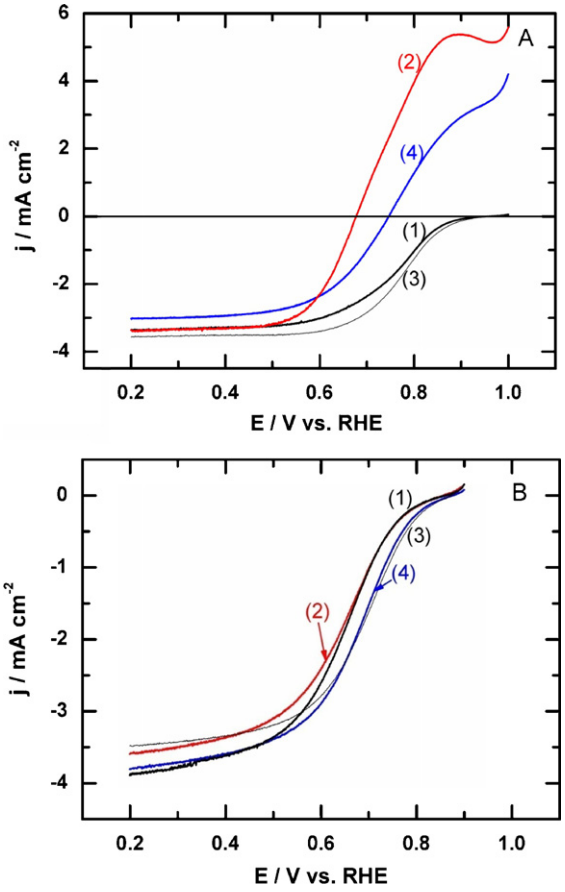

Fig. 6. Oxygen reduction reaction (ORR) curves at 900 rpm on (A) 8 wt% Pt/C (1 and 2) and 8 wt% Pt/5 wt% TiO_2/C (3 and 4) and on (B) 15 wt% Ru_xSe_y/C (1 and 2) and 15 wt% Ru_xSe_y/5 wt% TiO_2/C (3 and 4) in oxygen-saturated 0.5 M H_2SO_4 (curves 1 and 3) and in oxygen-saturated 5 M CH_3OH in 0.5 M H_2SO_4 (curves 2 and 4), at 25 °C. Scan rate of 5 mV s^{-1}.

3.2.2. ORR in sulfuric acid and pollutants containing sulfuric acid electrolyte

Fig. 5 depicts the ORR curves for Pt (A) and Ru_xSe_y (B) catalysts in 0.5 M sulfuric acid (curves 1 and 3) and in 5 M formic acid + 0.5 M sulfuric acid (curves 2 and 4). For Pt catalysts it is clear that the presence of formic acid strongly influences the ORR process as expected. The activity for the ORR in pure electrolyte is higher for 8 wt% Pt/5 wt% TiO_2/C than for 8 wt% Pt/C (Fig. 5A, curves 1 and 3), as reported previously [25], and its tolerance to formic acid is also improved by the presence of the oxide sites (curves 2 and 4). Its mixed-potential is shifted to a higher potential from 0.30 to 0.38 V/RHE as compared to the Pt/C catalyst.

As expected in the previous part, the Ru_xSe_y onto the oxide sites becomes more sensitive to oxidize the formic acid. This relatively enhanced oxidation process of the chalcogenide on the oxide with the ORR leads to a mixed-potential of 0.77 V/RHE, i.e., −90 mV shift with respect to Ru_xSe_y/C (Fig. 5B). In spite of this decrease of tolerance the Ru_xSe_y/5 wt% TiO_2/C catalyst is by far more tolerant to the presence of formic acid during the ORR process as compared to Pt catalyst. This trend is also observed for methanol tolerance.

Fig. 6A and B shows the ORR activity for the same catalysts in pure sulfuric acid electrolyte (curves 1 and 3) and in methanol-containing acid electrolyte (curves 2 and 4). The first observation for Pt based catalysts (Fig. 6A) is that the tolerance towards methanol is higher than for formic acid since the developed mixed-potentials are more positive, i.e., 0.68–0.72 V/RHE for 8 wt% Pt/C and 8 wt% Pt/5 wt% TiO_2/C, respectively, cf. Fig. 4A. The platinum centers deposited on oxide sites of the oxide–carbon composite are more

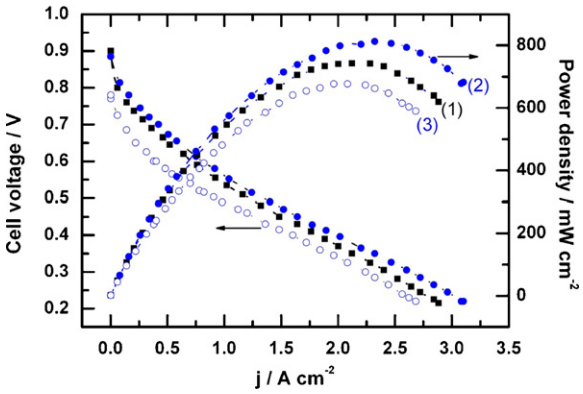

Fig. 7. H_2/O_2 PEMFC polarization curves and power density for (1) 8 wt% Pt/C, (2) 8 wt% Pt/5 wt% TiO_2/C and (3) 8 wt% Pt/5 wt% TiO_2/C cathode catalysts. 30 wt% Pt/C (E-TEK) was used as anode catalysts with a loading of 0.4 mg cm^{-2}. For cathode catalysts, the loading was 0.16 mg cm^{-2} (curves 1 and 2) and 0.4 mg cm^{-2} (curves 3) deposited on 5 cm^2. Tests were performed using a Nafion® 212 membrane at 80 °C. The flow rate of O_2 was 100 mL min^{-1} and 200 mL min^{-1} for H_2. Back pressure: 30 psi.

tolerant to the presence of methanol during the ORR (curves 2 and 4). However, full tolerance to methanol in the presence of molecular oxygen is observed by the chalcogenide material whether deposited or not on the oxide sites, see Fig. 5B, in agreement with previous works [48–50,76,77] and our discussion on the synergistic subtract effect (see Section 3.2.1). We observe for the first time that the same trend is obtained for Ru_xSe_y/TiO_2/C. This was confirmed with Laminar Flow Fuel Cell (LFFC) measurements, where a formic acid cross-over is observed from the anode to the cathode.

3.3. Fuel cell measurements

3.3.1. Single H_2/O_2

The 8 wt% Pt/C and 8 wt% Pt/5 wt% TiO_2/C catalysts were tested in a H_2/O_2 fuel cell. Fig. 7 displays the power density and polarization curves obtained for these tests. First, one can see, for the same cathode catalyst loading, i.e., 0.16 mg_{Pt} cm^{-2} (curves 1 and 2), that the platinum deposited on the composite exhibits higher performance than platinum deposited on carbon alone. The maximum power density obtained for the 8 wt% Pt/C is 750 mW cm^{-2} at 0.36 V and 816 mW cm^{-2} at 0.34 V for the 8 wt% Pt/5 wt% TiO_2/C. Depending on the Pt loading this power corresponds to 4.7 and 5 W mg_{Pt}^{-1}, respectively. Considering that the anode catalyst is the same, 30 wt% Pt/C E-TEK, 0.4 mg cm^{-2}, the observed enhancement of activity is consistent with the behavior observed for ORR. The substrate effect plays a role in fuel cell performance. Second, the thickness of the electrode in the Membrane Electrode Assembly (MEA) is also an important point for the fuel cell performance. In fact, if the thickness of the cathode increases by increasing the loading on the same surface, the performance decreases as shown in curves 2 and 3 (Fig. 7). The loading increases more than two times for the 8 wt% Pt/5 wt% TiO_2/C, and the power density is lower than the one obtained for the 8 wt% Pt/C.

3.3.2. Laminar-flow fuel cell measurements

Fig. 8 shows the polarization curves for the cathode catalysts: 8 wt% Pt/TiO_2/C, 8 wt% Pt/C and 10 wt% Pt/C (E-TEK) and for the anode catalyst: 30 wt% Pd/C E-TEK. The open circuit potential (OCP) of the cathode, when using Pt/C catalyst was 0.83 vs. RHE. For Pt/TiO_2/C and commercial Pt/C, the OCP was 14% higher and very close to the one that is usually measured in ORR electrochemical experiments with O_2-saturaded 0.5 M H_2SO_4 solution. The fact that the OCP is very close to the electrochemical value shows the effectiveness of the micro porous separator to reduce fuel cross-over. According to the provider, the micro-filter allows a cross-over

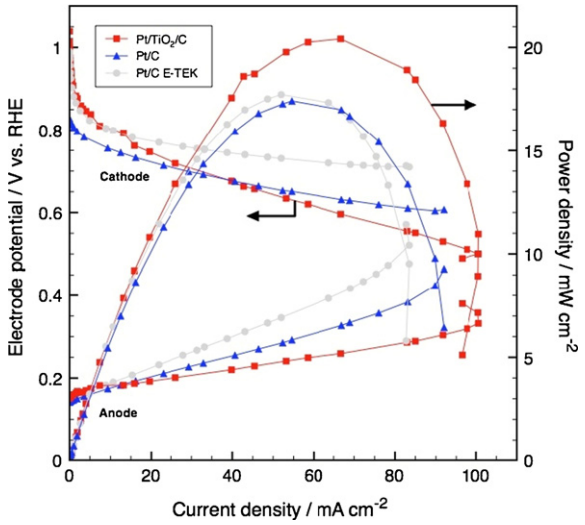

Fig. 8. Oxygen-breathing LFFC polarization curves for 8 wt% $Pt/TiO_2/C$, 8 wt% Pt/C and 10 wt% Pt/C (E-TEK) cathode catalysts. An anode 30 wt% Pd/C (E-TEK) was used. The voltage of cathode and anode was measured separately and the power density is plotted with respect to right vertical axis. Tests were performed using 5 M HCOOH + 0.5 M H_2SO_4 as anolythe and 0.5 M H_2SO_4 as catholyte. The flow rate of the inlet streams was 0.5 mL min^{-1}.

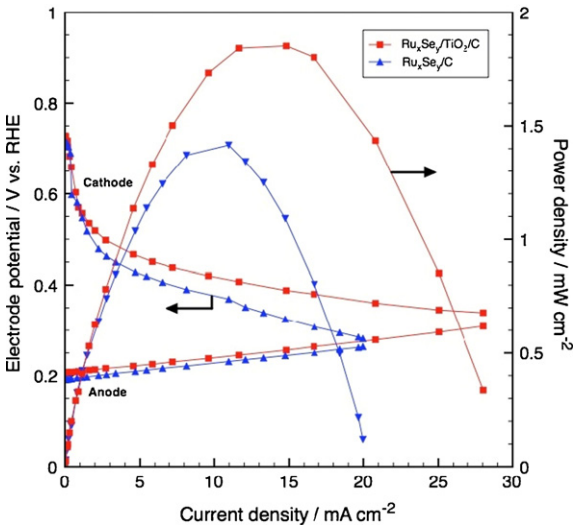

Fig. 9. Oxygen-breathing LFFC polarization curves for 15 wt% $Ru_xSe_y/TiO_2/C$ and 15 wt% Ru_xSe_y/C cathode catalysts. An anode 30 wt% Pd/C (E-TEK) was used. The voltage of cathode and anode was measured separately and the power density is plotted with respect to the right vertical axis. Tests were performed using 5 M HCOOH + 0.5 M H_2SO_4 as anolythe and 0.5 M H_2SO_4 as catholyte. The flow rate of the inlet streams was 0.5 mL min^{-1}.

flow of water of 18 mL min^{-1} cm^{-2} [78]. While such parameter is unknown for 0.5 M HCOOH + 0.5 M H_2SO_4, it clearly affects the concentration gradient of formic acid in the catholyte, reducing the amount of organic molecules on the surface of the cathode. We have reported how the open circuit voltage (OCV) of a microfluidic fuel cell dramatically becomes lower as the presence of formic acid molecules are higher on the surface of a Pt/C cathode. The OCP of the anode remains the same, ca. 150 mV vs. RHE, for all tested cathode materials. This value agrees well with the onset potential of HCOOH oxidation by nanostructured Pd catalyst, in N_2-purged 0.5 M HCOOH + 0.5 M H_2SO_4 solution.

At cathode potentials lower than 0.8 V, begins the section of typical flow fuel cell curves known as mixed-control region. Herein, a competition between the rate of oxidation of HCOOH molecules and the rate of reduction of O_2 molecules exists. Such delicate equilibrium affects the potential of both electrodes. This potential is also influenced by the ease with which the reactive molecules are transported into the depletion zone on the surface of the electrode. The entire process is not controlled by the cathode nor the anode alone. It is only when the total potential of the cell is measured, i.e. $E_{cat} - E_{an}$, that one can realize that the performance of LFCC with $Pt/TiO_2/C$ as cathode exceeds that of their counterparts that do not use a composite support. At ca. 52 mA cm^{-2} a peak specific power density of 17.4 mW cm^{-2} is obtained for the catalysts supported only on carbon. No appreciable difference between the commercial one and the one synthesized via carbonyl was found. For cathodes with $Pt/TiO_2/C$ catalyst, this peak attains 20.4 mW cm^{-2} at 66.7 mA cm^{-2}. The attained specific power is 17% higher than that obtained with Pt/C catalyst. These results are in good agreement to the ones discussed in Section 3.2, and they are a consequence of the enhanced activity and tolerance using an oxide–carbon composite support.

As $E_{cat} - E_{an}$ decreases 200 mV, mass transport issues start to appear for the anode (see Fig. 8). When the difference in potential becomes smaller, the current starts to decrease instead of continuing to increase. While the potential becomes more positive for the anode, it becomes more positive for the cathode. Thus, the current values always correspond to their respective potential ones. This is not surprising since the commercial catalyst is known to have big particle size and a poor distribution on the support too.

The polarization curves for the cathode catalysts: $Ru_xSe_y/TiO_2/C$, Ru_xSe_y/C, and for the anode catalyst: Pd/C, are shown in Fig. 9. The measured OCP was 0.72 V vs. RHE and 0.2 V vs. RHE for the cathode and anode, respectively. As the resistance of the load is increased, $E_{cat} - E_{an}$ decreases. However, $\Delta E/\Delta j$ is 9% lower for $Ru_xSe_y/TiO_2/C$ than for Ru_xSe_y/C. This result puts in evidence the improvement of the ORR kinetics by the chalcogenide supported on TiO_2/C rather than on carbon alone. Throughout the kinetics, mixed-control and mass transport regions of the polarization process, the anode curves are parallel and almost the same. On the other hand, the cathode curves differ from each other and this difference is very similar to the one obtained during the ORR experiments (see Figs. 5 and 6). Therefore, the performance of the LFFC is clearly controlled by the cathode, not by the anode. Additionally, the fact that the OCP was the same for $Ru_xSe_y/TiO_2/C$ and for Ru_xSe_y/C puts in evidence that both inlet streams are well separated and fuel-crossover negative effects are not relevant at this concentration of HCOOH. Consequently, the increase of specific current in $Ru_xSe_y/TiO_2/C$ polarization curve is exclusively due to the higher ORR activity and improvement in mass transport of this catalyst. A maximum specific power of 1.85 mW cm^{-2} and 1.41 mW cm^{-2} was obtained for $Ru_xSe_y/TiO_2/C$ and Ru_xSe_y/C, respectively. This corresponds to 24% performance improvement of the LFFC when using TiO_2/C as support for the cathode catalysts.

4. Conclusions

The ORR study and fuel cell tests (PEMFC: H_2/O_2) confirmed the enhancement of the catalytic activity of platinum supported on the oxide–carbon composite prepared by photo-deposition. The same observation was done for the tolerance towards formic acid and methanol. It appears that the Ru_xSe_y supported catalysts do not follow the same trend in terms of tolerance towards these molecules, but fuel cell performances are not affected by this phenomenon. The LFFC with cathodes of $Pt/TiO_2/C$ and $Ru_xSe_y/TiO_2/C$ produced a maximum output specific power of 20.4 and 1.85 W g^{-1}, respectively. This corresponds to 15% more power for the Pt catalyst supported on the semiconductor and 24% for the chalcogenide in comparison with the TiO_2-free cathodes. These results are a direct consequence of the enhanced catalytic activity and tolerance.

Acknowledgments

L. Timperman was supported by a fellowship of the "Ministère de l'Enseignement Supérieur et Recherche". A.S. Gago thanks CONACYT for financial support (Scholarship 305477).

References

[1] A. Kongkanand, S. Kuwabata, G. Girishkumar, P. Kamat, Langmuir 22 (2006) 2392.
[2] G. Vijayaraghavan, K.J. Stevenson, Langmuir 23 (2007) 5279.
[3] S. Maldonado, K.J. Stevenson, J. Phys. Chem. B 109 (2005) 4707.
[4] P.H. Matter, L. Zhang, U.S. Ozkan, J. Catal. 239 (2006) 83.
[5] L. Calvillo, M.J. Lázaro, E. García-Bordejé, R. Moliner, P.L. Cabot, I. Esparbé, E. Pastor, J.J. Quintana, J. Power Sources 169 (2007) 59.
[6] E. Guilminot, F. Fischer, M. Chatenet, A. Rigacci, S. Berthon-Fabry, P. Achard, E. Chainet, J. Power Sources 166 (2007) 104.
[7] P.H. Matter, E. Wang, M. Arias, E.J. Biddinger, U.S. Ozkan, J. Mol. Catal. A: Chem. 264 (2007) 73.
[8] E.P. Ambrosio, C. Francia, M. Manzoli, N. Penazzi, P. Spinelli, Int. J. Hydrogen Energy 33 (2008) 3142.
[9] X.L. Chen, W.S. Li, C.L. Tan, W. Li, Y.Z. Wu, J. Power Sources 184 (2008) 668.
[10] E. Guilminot, R. Gavillon, M. Chatenet, S. Berthon-Fabry, A. Rigacci, T. Budtova, J. Power Sources 185 (2008) 717.
[11] M. Lefèvre, J.-P. Dodelet, Electrochim. Acta 53 (2008) 8269.
[12] B. Fang, J.H. Kim, M. Kim, J.-S. Yu, Chem. Mater. 21 (2009) 789.
[13] B. Seger, A. Kongkanand, K. Vinodgopal, P.V. Kamat, J. Electroanal. Chem. 621 (2008) 198.
[14] K. Sasaki, L. Zhang, R.R. Adzic, Phys. Chem. Chem. Phys. 10 (2008) 159.
[15] N.R. Elezovic, B.M. Babic, V.R. Radmilovic, L.M. Vracar, N.V. Krstajic, Electrochim. Acta 54 (2009) 2404.
[16] P. Kulesza, K. Miecznikowski, B. Baranowska, M. Skunik, A. Kolary-Zurowska, A. Lewera, K. Karnicka, M. Chojak, I. Rutkowska, S. Fiechter, P. Bogdanoff, I. Dorbandt, G. Zehl, R. Hiesgen, E. Dirk, K. Nagabhushana, H. Boennemann, J. Appl. Electrochem. 37 (2007) 1439.
[17] M.S. Saha, M.N. Banis, Y. Zhang, R. Li, X. Sun, M. Cai, F.T. Wagner, J. Power Sources 192 (2009) 330.
[18] T. Matsui, K. Fujiwara, T. Okanishi, R. Kikuchi, T. Takeguchi, K. Eguchi, J. Power Sources 155 (2006) 152.
[19] J. Shim, C.-R. Lee, H.-K. Lee, J.-S. Lee, E.J. Cairns, J. Power Sources 102 (2001) 172.
[20] L. Xiong, A. Manthiram, Electrochim. Acta 49 (2004) 4163.
[21] M. Gustavsson, H. Ekström, P. Hanarp, L. Eurenius, G. Lindbergh, E. Olsson, B. Kasemo, J. Power Sources 163 (2007) 671.
[22] X.-Y. Xie, Z.-F. Ma, X. Wu, Q.-Z. Ren, X. Yuan, Q.-Z. Jiang, L. Hu, Electrochim. Acta 52 (2007) 2091.
[23] N.R. de Tacconi, C.R. Chenthamarakshan, K. Rajeshwar, W.-Y. Lin, T.F. Carlson, L. Nikiel, W.A. Wampler, S. Sambandam, V. Ramani, J. Electrochem. Soc. 155 (2008) B1102.
[24] S. von Kraemer, K. Wikander, G. Lindbergh, A. Lundblad, A.E.C. Palmqvist, J. Power Sources 180 (2008) 185.
[25] L. Timperman, N. Alonso-Vante, Electrocatalysis, submitted for publication.
[26] W. Vogel, L. Timperman, N. Alonso-Vante, Appl. Catal. A 377 (2010) 167.
[27] L. Timperman, Y.J. Feng, W. Vogel, N. Alonso-Vante, Electrochim. Acta 55 (2010) 7558.
[28] H. Zhang, W. Zhou, Y. Du, P. Yang, C. Wang, J. Xu, Int. J. Hydrogen Energy, doi:10.1016/j.ijhydene.2010.09.025.
[29] C. Chen, F. Pan, Appl. Catal. B: Environ. 91 (2009) 663.
[30] S. Yoo, T. Jeon, K. Lee, K. Park, Y. Sung, Chem. Commun. 46 (2010) 794.
[31] E. Formo, Z. Peng, E. Lee, X. Lu, H. Yang, Y. Xia, J. Phys. Chem. C 112 (2008) 9970.
[32] G. Selvarani, S. Maheswari, P. Sridhar, S. Pitchumani, A.K. Shukla, J. Electrochem. Soc. 156 (2009) B1354.
[33] J. Croy, S. Mostafa, J. Liu, Y. Sohn, H. Heinrich, B. Cuenya, Catal. Lett. 119 (2007) 209.
[34] X. Wang, J. Wang, Q. Zou, Y. Xia, Electrochim. Acta, doi:10.1016/j.electacta.2010.08.003.
[35] A. Kundu, J. Jang, J. Gil, C. Jung, H. Lee, S. Kim, B. Ku, Y. Oh, J. Power Sources 170 (2007) 67.
[36] T.S. Zhao, W.W. Yang, R. Chen, Q.X. Wu, J. Power Sources 195 (2010) 3451.
[37] S.K. Kamarudin, F. Achmad, W.R.W. Daud, Int. J. Hydrogen Energy 34 (2009) 6902.
[38] A. Blum, T. Duvdevani, M. Philosoph, N. Rudoy, E. Peled, J. Power Sources 117 (2003) 22.
[39] T. Aoki, A. Matsunaga, Y. Ogami, A. Maekawa, J. Power Sources 195 (2010) 2182.
[40] E. Choban, L. Markoski, A. Wieckowski, P. Kenis, J. Power Sources 128 (2004) 54.
[41] R.S. Jayashree, S.K. Yoon, F.R. Brushett, P.O. Lopez-Montesinos, D. Natarajan, L.J. Markoski, P.J.A. Kenis, J. Power Sources (2010) 1.
[42] D. Whipple, R. Jayashree, D. Egas, N. Alonso-Vante, P. Kenis, Electrochim. Acta 54 (2009) 4384.
[43] K. Scott, A. Shukla, C. Jackson, W. Meuleman, J. Power Sources 126 (2004) 67.
[44] Y. Gochi-Ponce, G. Alonso-Nunez, N. Alonso-Vante, Electrochem. Commun. 8 (2006) 1487.
[45] Y. Feng, T. He, N. Alonso-Vante, Fuel Cells 10 (2009) 77.
[46] N. Alonso-Vante, in: W. Vielstich, A. Lamn, H. Gasteiger (Eds.), Handbook of Fuel Cells – Fundamentals, Technology and Applications, John Wiley & Sons, Ltd., Chichester, U.K., 2003, p. 534.
[47] V.I. Zaikovskii, K.S. Nagabhushana, V.V. Kriventsov, K.N. Loponov, S.V. Cherepanova, R.I. Kvon, H. Bonnemann, D.I. Kochubey, E.R. Savinova, J. Phys. Chem. B 110 (2006) 6881.
[48] N. Alonso-Vante, Fuel Cells 6 (2006) 182.
[49] S.A. Campbell, US Patent 2004/0096728 A1, US Patent 2004/0096728 A1 (2004).
[50] C. Delacote, A. Bonakdarpour, C.M. Johnston, P. Zelenay, A. Wieckowski, Faraday Discuss. 140 (2009) 269.
[51] A.S. Hollinger, R.J. Maloney, R.S. Jayashree, D. Natarajan, L.J. Markoski, P.J.A. Kenis, J. Power Sources (2010) 1.
[52] D.T. Whipple, R.S. Jayashree, D. Egas, N. Alonso-Vante, P.J.A. Kenis, Electrochim. Acta 54 (2009) 4384.
[53] R.S. Jayashree, L. Gancs, E.R. Choban, A. Primak, D. Natarajan, L.J. Markoski, P.J.A. Kenis, J. Am. Chem. Soc. 127 (2005) 16758.
[54] A. Capon, R. Parson, J. Electroanal. Chem. 44 (1973) 1.
[55] A. Capon, R. Parsons, J. Electroanal. Chem. 45 (1973) 205.
[56] G.-Q. Lu, A. Crown, A. Wieckowski, J. Phys. Chem. B 103 (1999) 9700.
[57] X. Wang, J.-M. Hu, I.M. Hsing, J. Electroanal. Chem. 562 (2004) 73.
[58] R.S. Jayashree, J.S. Spendelow, J. Yeom, C. Rastogi, M.A. Shannon, P.J.A. Kenis, Electrochim. Acta 50 (2005) 4674.
[59] J.D. Lovic, A.V. Tripkovic, S.L. Gojkovic, K.D. Popovic, D.V. Tripkovic, P. Olszewski, A. Kowal, J. Electroanal. Chem. 581 (2005) 294.
[60] J.-H. Choi, K.-J. Jeong, Y. Dong, J. Han, T.-H. Lim, J.-S. Lee, Y.-E. Sung, J. Power Sources 163 (2006) 71.
[61] V. Selvaraj, M. Alagar, K.S. Kumar, Appl. Catal. B 75 (2007) 129.
[62] Z.-Z. Zhu, Z. Wang, H.-L. Li, Appl. Surf. Sci. 254 (2008) 2934.
[63] V. Selvaraj, A.N. Grace, M. Alagar, J. Colloid Interface Sci. 333 (2009) 254.
[64] W. Zhou, Y. Du, H. Zhang, J. Xu, P. Yang, Electrochim. Acta 55 (2010) 2911.
[65] J.D. Lovic, A.V. Tripkovic, S.L.J. Gojkovic, K.D. Popovic, D.V. Tripkovic, P. Olszewski, A. Kowal, J. Electroanal. Chem. 581 (2005) 294.
[66] M. Arenz, V. Stamenkovic, K. Wandelt, P.N. Ross, N.M. Markovic, Phys. Chem. Chem. Phys. 5 (2003) 4242.
[67] X. Zhou, C. Liu, J. Liao, T. Lu, W. Xing, J. Power Sources 179 (2008) 481.
[68] Z. Liu, X. Ling, X. Su, J. Lee, J. Phys. Chem. B 108 (2004) 8234.
[69] M. Hepel, I. Dela, T. Hepel, J. Luo, C. Zhong, Electrochim. Acta 52 (2007) 5529.
[70] S. Tauster, S. Fung, R. Garten, J. Am. Chem. Soc. 100 (1978) 170.
[71] J. Horsley, J. Am. Chem. Soc. 101 (1979) 2870.
[72] L. Timperman, A. Lewera, W. Vogel, N. Alonso-Vante, Electrochem. Commun. 12 (2010) 1772.
[73] M.S. Spencer (Ed.), Strong Metal–Support Interactions, vol. 298, American Chemical Society, 1986, p. 89.
[74] M. Jeon, P. McGinn, J. Power Sources 195 (2010) 2664.
[75] W. Vogel, Personal communication.
[76] N. Alonso-Vante, P. Bogdanoff, H. Tributsch, J. Catal. 190 (2000) 240.
[77] L.G. Arriaga, Y. Gochi, N. Alonso Vante (Eds.), ECS 210th, 2006.
[78] http://www.millipore.com/catalogue/itemdetail.do?id=GSWP01300.